Behavior of rubidium at over eightfold static compression

Behavior of Rubidium at Over 8-fold Static Compression

C. V. Storm,* J. D. McHardy, S. E. Finnegan, E. J. Pace, M. G. Stevenson, M. J. Duff, and M. I. McMahon
SUPA, School of Physics and Astronomy, and Centre for Science at Extreme Conditions, The University of Edinburgh, Peter Guthrie Tait Road, Edinburgh EH9 3FD, United Kingdom

S. G. MacLeod
AWE, Aldermaston, Reading, RG7 4PR, United Kingdom and
SUPA, School of Physics and Astronomy, and Centre for Science at Extreme Conditions, The University of Edinburgh, Peter Guthrie Tait Road, Edinburgh EH9 3FD, United Kingdom
(Dated: September 6, 2021)

The high pressure phases of rubidium have previously been investigated to 101 GPa, above which Rb is predicted to adopt a double-hexagonal close-packed (*dhcp*, Pearson $hP4$) structure similar to that already observed in cesium at 72 GPa. Previous *ab initio* structure searches have indicated that the $hP4$ phase should become stable in rubidium at 143 GPa. We present data from static compression experiments on Rb up to 264(8) GPa, showing the onset of the $hP4$ phase at 207(6) GPa. The V/V_0 of ~ 0.121 measured at 264 GPa constitutes the highest compression ratio (>8-fold) at which structural information has been obtained from a metal using x-ray diffraction methods and is second only to x-ray measurements performed on hydrogen at a $V/V_0 \sim 0.094$ at 190 GPa. At these extreme compression ratios, the compressive behavior of rubidium shifts from that of a free electron metal to that of a regular d-block metal.

I. INTRODUCTION

The alkali metals have long been of great interest due to their simple crystallographic and electronic structure. Their single valence electron makes them a good approximation of the nearly-free electron (NFE) model at ambient conditions [1, 2]. Under pressure, however, these simple metals become increasingly complex; while all adopt a body-centered cubic structure at ambient pressure and subsequently transform to a face-centered cubic structure under modest pressure, further compression results in a multitude of complex, electride-like and host-guest composite structures [3–5].

This transition from simple to complex structures must result from a lowering of the electronic energy, which in turn is generally understood to originate from a structural distortion which splits degenerate states at the Fermi level [6, 7]. However, the driving force of such distortions remains contested; an often-cited cause is the localization of valence electrons in interstitial sites under pressure [8–10]. This lowers the bandwidth and makes Peierls-like distortions favorable, lowering both symmetry and the electronic energies [11]. On the other hand, these low-symmetry structures may result from Hume-Rothery rules [12], wherein interactions between the Fermi surface and the Brillouin zone cause energy gaps to open near the Fermi level [13–16] similarly reducing the electronic energy.

Regardless, it is well-documented that upon compression there occurs an s-d charge transfer, where the d-character of the electron bands is strengthened under pressure [17–20]. If this was the *only* effect of compression, then the alkalis should indeed become increasingly free-electron like under pressure and adopt further close-packed structures once the s-d transfer is complete [21]. However, this is not the case as the high-pressure phases of the alkalis show a wealth of complexity (see Table I for an overview and Ref. [22] for a full review).

It has furthermore been observed that elements within the same group (e.g. group I for the alkali metals) will adopt similar structures at high pressure, with the phase transition pressures being lower in the higher-Z group members as illustrated for the alkali metals in Table I. For materials undergoing changes in electronic structure it is also known that the atomic volume and compressibility of a lower-Z metal can tend towards that of its neighbor in the next group. For instance, the compression curve of scandium ($Z = 21$) has been observed to tend towards that of titanium ($Z = 22$) above 200 GPa [23], while the compressibility of divalent europium ($Z = 63$) approaches that of trivalent gadolinium ($Z = 64$) at 20 GPa [24].

By analogy then, one might expect the compressibility and atomic volume of rubidium (Rb, $Z = 37$) to approach the behavior of its closest neighbors strontium (Sr, $Z = 38$) and yttrium (Y, $Z = 39$) as a result of the s-d charge transfer. Since experimental compression data for Sr only exist up to 75 GPa [25], we will focus here on Y which we have recently studied up to 180 GPa [26].

In another parallel between Rb and Y, our recent experimental studies have indicated that Y also tends towards d-like behavior at ultra-high pressures [26]. However, with an ambient bulk modulus of 47.3 GPa, the relative incompressibility of Y limited the accessible compression domain to $V/V_0 > 0.35$, even at a few hundreds of GPa. The alkali metals on the other hand are extraordinarily compressible, with the zero-pressure bulk moduli of the heavier alkali metals potassium (K), rubidium (Rb), and cesium (Cs) being 3.1 GPa, 2.5 GPa and

* christian.storm@ed.ac.uk

Element	Transition Sequence	
K	$bcc \xrightarrow{11.6} fcc \xrightarrow{20}$ *h-g* ($tI19$*) $\xrightarrow{54} oP8 \xrightarrow{90} tI4 \xrightarrow{96} oC16$	<112 GPa
Rb	$bcc \xrightarrow{7.0} fcc \xrightarrow{13} oC52 \xrightarrow{14}$ *h-g* ($tI19$*) $\xrightarrow{20} tI4 \xrightarrow{48} oC16$	<100 GPa
Cs	$bcc \xrightarrow{2.4} fcc \xrightarrow{4.2} oC84 \xrightarrow{4.3} tI4 \xrightarrow{12} oC16 \xrightarrow{72} hP4$	<223 GPa

TABLE I. The phase transition sequences observed in the three heavier alkali metals K, Rb and Cs. Above the common *bcc* and *fcc* phases seen in all three metals at low pressures, the crystal structures are given by their Pearson symbols, with host-guest structures abbreviated *h-g*. The asterisks denote that the number of atoms in the host-guest structures is non-integer and pressure-dependent. Numbers above the arrows indicate the transition pressures in GPa. Table adapted from Ref. [16].

1.6 GPa, respectively, only 2-3 times larger than those of the solidified noble gases at ambient pressure and low temperature. As a result, the proportion of the sample volume occupied by the relatively incompressible ion cores in the alkali metals increases rapidly under pressure until the distance between them decreases below the initial core diameter. Such so-called 'core-core' overlap forces the valence electrons to localize into irregularly-shaped interstitial regions [8, 9].

These localized electrons can act as almost massless pseudo-anions, resulting in high-density "electride" structures and transitions to insulating or semiconducting forms [3]. While the effects of electron localization and hybridization apply to all high-density matter [27], the physics is most evident in the alkali metals, due to their NFE behavior at ambient conditions and the ease with which their densities can be increased more than 5-fold, thereby strongly reducing the volume accessible to the valence electrons and increasing interactions between core electrons.

All of these pressure-induced effects lead to the structural complexity shown in Table I, which contains the known high-pressure phase transitions in K, Rb and Cs and illustrates that these elements share many common structures, as expected given their similar electronic structures. In particular, the superconductive orthorhombic $oC16$ phase [28] becomes energetically favorable in K, Rb and Cs at pressures of 96 GPa, 48 GPa and 12 GPa, respectively [29–31]. Cs has also been observed to adopt a double-hexagonal close-packed (*dhcp*, Pearson $hP4$) structure at 72 GPa [32] and *ab initio* structure searches have indicated that Rb should also transform to an analogous $hP4$ structure at 143 GPa at 0 K [33].

To this end, we describe structural studies of Rb up to 264 GPa at 300 K and observe the transition to the $hP4$ phase at 207(6) GPa. Analysis of Rb's equation of state (EoS) shows a marked decrease in compressibility between 25 and 30 GPa, within the $tI4$ phase, where the atomic volume becomes very similar to that of Y. Above 30 GPa Rb behaves far more like a regular *d*-type metal, i.e. a metal whose valence electrons are primarily in a *d*-configuration. This agrees with theoretical conclusions that at such pressures the *d*-character of Rb's electron bands will dominate. At 264 GPa, the density of Rb is more than 8-times its ambient pressure value, and the nearest neighbor distance is only 2.51 Å, significantly smaller than the Rb^+ ionic diameter of 3.04 Å [34] and thereby confirming that we have reached the density domain where core-core overlap is an important consideration.

II. EXPERIMENTAL METHOD

Commercial Rb samples of high purity (99.95 %+) supplied by Sigma-Aldrich were loaded into Boehler-Almax design plate diamond anvil cells [35]. Due to the highly reactive nature of Rb, all samples were prepared in a dry oxygen-free atmosphere (<0.1ppm O_2 and <0.1ppm H_2O) and no pressure transmitting medium was used.

Data below 7 GPa were collected on beamline P02.2 at PETRA-III with a wavelength of 0.4840 Å and a beam size of 3 µm × 8 µm. Diamond anvils cells with 500 µm diameter culets were employed, along with a rhenium (Re) gasket, and pressure was determined from copper (Cu) powder scattered throughout the sample chamber and the Cu EoS [36].

Between 7 GPa and 25 GPa data were collected on beamline I15 at the Diamond Light Source (DLS) with a wavelength of 0.4246 Å and a beam size of approximately 20 µm × 20 µm. Here, diamond anvil cells with 100 µm diameter culets were used, beveled at 8.5° to 300 µm. A small piece of tantalum (Ta) foil served as the pressure calibrant using the Ta EoS [36], and the gasket was Re.

Data above 25 GPa were collected during two experiments on beamline P02.2 at PETRA-III, the first with a 3 µm × 8 µm beam size (wavelength 0.4840 Å) and the second with a 850 nm × 850 nm beam size (wavelength 0.4855 Å) enabled by the facility's sub-micron focus [37].

While the nano-focused beam provided diffraction patterns with less interference from the gasket, the highest pressure was reached while using the larger beam. Furthermore, we were unable to obtain pressure measurements from the sample studied with the sub-micron beam and therefore relied on a derived Rb EoS from the first experiment to determine the pressure in Figs. 2 & 3. No data from the sub-micron experiment are therefore shown in Figs. 4-6.

The high-pressure diamond anvils had 30 µm diameter culets beveled at 8.5° to 300 µm. The gaskets were Re, and no *in-situ* pressure calibrants were used as the

Facility	Range (GPa)	λ (Å)	Beam (μm^2)	Diffraction Standard	Pressure Calibrant	d (mm)
P-III	0-7	0.4840	3×8	CeO_2	Cu	395
DLS	7-25	0.4246	20×20	LaB_6	Ta	299
P-III	25-264	0.4840	3×8	CeO_2	*DE*	395
P-III	25-232	0.4855	0.85×0.85	CeO_2	None	396

TABLE II. Calibration parameters giving the pressure range, the x-ray wavelength (λ), the x-ray beam diameter, the calibration standard, the pressure gauge, and the sample-detector distance (d). The diamond Raman high-frequency edge method is abbreviated *DE*, and we have abbreviated PETRA-III to P-III.

diffraction signal would have obscured that of the sample; the pressure was instead determined from the diamond anvil Raman gauge [38–40] (see Figs. S2, S3, and S4 in the Supplementary Material for a discussion of pressure gradients on the culet surface and for a sample Raman spectrum from which the pressure was determined [41]). Since this pressure gauge is only calibrated above 100 GPa, the pressures for data collected below this point were estimated from the diffraction signal of the Re gasket using its EoS [42]. Given the small beam size relative to the ∼5 µm diameter of the sample chamber the diffraction from the gasket originated primarily from gasket material in contact with the sample and thus provides a reasonable pressure estimate. We include experimental results from Refs. [30, 43, 44] in Figs. 4-6 to show agreement with these studies to support the assumption that the Re gasket provides a reasonable pressure estimate.

The diffraction data were recorded on a Perkin-Elmer area detector (PETRA-III) and a MAR345 image-plate detector (DLS). At PETRA-III the detector was placed ∼400 mm from the sample, and at DLS it was placed ∼300 mm from the sample. The exact sample-detector distance and the detector tilts were determined using diffraction standards (LaB_6, CeO_2). A summary of the calibration parameters and beamline arrangements is shown in Table II.

An example of the quality of the diffraction data obtained is illustrated in Fig. 1 which shows the 2D diffraction image collected at 232 GPa. There is only minimum scattering from the Re gasket, and there are no diffraction features from the diamond anvils. The 2D diffraction images obtained at each pressure were integrated to 1D profiles using DIOPTAS [45], and these were analyzed using Rietveld and Le Bail profile fitting [46], and least-squares fitting to individual peak positions [47].

The sample pressures were increased manually and allowed to stabilize for at least 5 min before the x-ray exposures were taken. The typical exposure time was 60 s.

III. RESULTS

Our observed phase transitions up to 50 GPa are shown in Table III along with the respective transition pressures, and these are all in good agreement with previous investigations [44, 48, 49] (see Table I).

A. Phases and Refinement

The quality of the diffraction data collected above 150 GPa is demonstrated in Fig. 2 which shows a background-subtracted diffraction profile from the $oC16$ phase at 189 GPa, along with a Rietveld profile refinement. The refined lattice parameters at this pressure were $a = 8.282(6)$ Å, $b = 4.920(2)$ Å, $c = 4.9170(10)$ Å ($V = 12.522(11)$ Å^3/atom), with atoms on the *8f* and *8d* Wyckoff sites of space group *Cmca* at (0,0.180(5),0.327(7)) and (0.216(4),0,0), respectively. The atomic coordinates were unchanged over the full stability range of this phase and are in excellent agreement with the theoretical values of *8f* (0,0.1751,0.3271) and *8d* (0.2149,0,0) [33].

On pressure increase above 189 GPa, additional diffraction peaks appeared in the diffraction profiles, as seen by comparing profiles (a) and (b) of Fig. 3. However, while the intensities of the new peaks increased with increasing pressure (profiles (c) and (d) of Fig. 3), peaks from

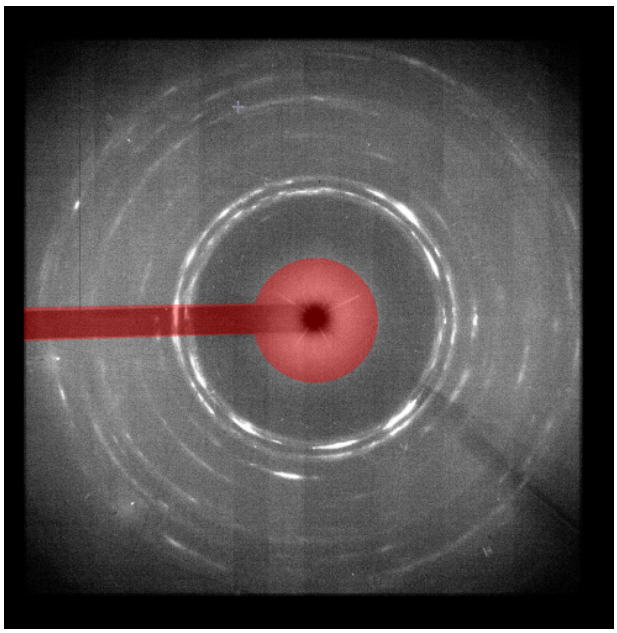

FIG. 1. The 2D Debye-Scherrer diffraction image from Rb at 232 GPa as collected with the 850 nm × 850 nm x-ray beam at PETRA-III. The masked sections are shown as shaded areas, with the rectangular mask corresponding to the mounting arm for the beam stop and the central circular mask to the beam stop itself.

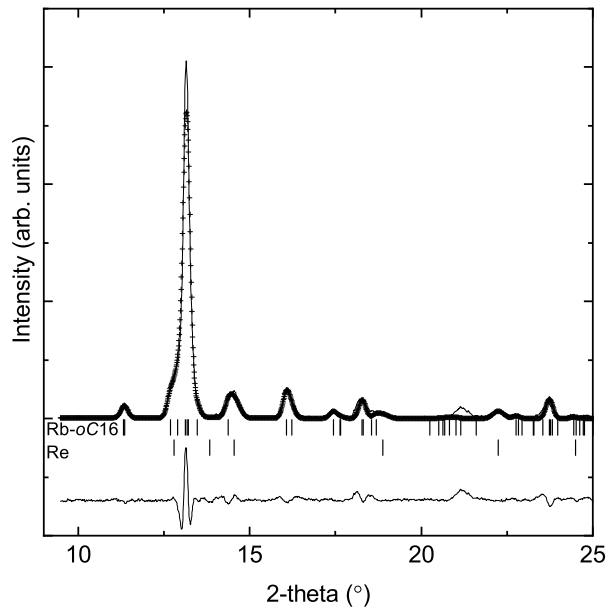

FIG. 2. Rietveld refinement of the $oC16$ structure to a background-subtracted diffraction profile from Rb at 189 GPa, showing the observed (solid line) and calculated (crosses) diffraction patterns. The collection time of the diffraction image was 60 s and the sample was not oscillated during exposure. The calculated reflection positions (vertical bars) for the $oC16$ phase (Rietveld) and Re gasket (Le Bail), and the difference profile (lower line), are also shown. Owing to the sub-micron x-ray beam the Re diffraction signal is very weak.

Rb-$oC16$ were still observed at 264(8) GPa, the highest pressure reached in this study before diamond failure.

The positions of the new peaks are consistent with those expected from $hP4$, which previous *ab initio* density functional theory (DFT) calculations had predicted would become stable above 143 GPa at 0 K [33]. It is then clear that temperature effects raise the transition pressure to this phase by around 60 GPa.

Although the mixed-phase nature of the diffraction profiles above 189 GPa precluded Rietveld analysis, Le Bail refinement at 222 GPa (see profile (c) in Fig. 3) gave best fitting values of $a = 8.2204(4)$ Å, $b = 4.802(2)$ Å, $c = 4.7907(17)$ Å, $V = 11.796(9)$ Å^3/atom for the $oC16$ phase and $a = 2.5239(7)$ Å, $c = 8.324(7)$ Å, $V = 11.48(11)$ Å^3/atom for the $hP4$ phase. There is thus a volume discontinuity of 2.3(5) % at the $oC16 \rightarrow hP4$ transition, similar to the 2.0(1) % volume decrease observed in the analogous $oC16 \rightarrow hP4$ transition in Cs at 72 GPa [32].

Transition		Pressure (GPa)
bcc (Rb-I)	→ *fcc* (Rb-II)	7.6(3)
fcc (Rb-II)	→ $oC52$ (Rb-III)	13.6(5)
$oC52$ (Rb-III)	→ *h-g*, $tI19^*$ (Rb-IV)	17.4(4)
h-g, $tI19^*$ (Rb-IV)	→ $tI4$ (Rb-V)	20.1(4)
$tI4$ (Rb-V)	→ $oC16$ (Rb-VI)	48.5(15)

TABLE III. Phases of Rb and their conventional numbered labels, as well as transition pressures observed in this study of Rb up to 50 GPa. The pressures are in good agreement with those reported in previous studies (see Refs. [44, 48, 49]).

Theoretical investigations have shown that following the $oC16 \rightarrow hP4$ transition the enthalpies of these two phases diverge by approximately 2 meV/atom/GPa in Cs [32], compared to 1.1 meV/atom/GPa in Rb [33]. With these phases coexisting across a range of ∼27 GPa in Cs [32], the lower divergence rate calculated for Rb matches our observed region of phase overlap of at least 60 GPa.

At 264 GPa the refined lattice parameters of the $hP4$ phase are $a = 2.5070(14)$ Å and $c = 8.258(17)$ Å, and the shortest Rb-Rb interatomic distance is then 2.507 Å. This implies not only that there is strong core-valence overlap, as the *5s* and *4p* radii are 2.287 Å and 0.735 Å respectively [50], but also significant core-core overlap between neighboring Rb atoms as the ionic diameter of Rb is 3.04 Å [34].

B. Compression

The extraordinary compressibility of Rb is demonstrated in Fig. 4, which shows the measured atomic volume to 264 GPa, where the reduced volume (V/V_0) is only 0.121. It is worth noting that even the initial *bcc-fcc* phase transition at 7.6(3) GPa occurs at a reduced volume of $V/V_0 < 0.5$. The ambient volume V_0 was determined by fitting a Vinet [51] EoS using EoSFit [52] to the low-pressure data from the *bcc* phase over the pressure range 0.051-7 GPa. See Fig. S1 in the Supplementary Material for full details on the Vinet fit [41]. This resulted in $V_0 = 92.9(4)$ Å^3/atom, $K_0 = 2.46(7)$ GPa, and $K' = 4.12(6)$, in excellent agreement with previous studies which obtained values of 92.74 Å^3/atom, 2.301(3) GPa, and 4.1(3) , respectively [49].

Also shown in Fig. 4 are the recently determined compression data of Y to 189 GPa [26]. At lower pressures, the compression curves of Rb ($Z = 37$) and Y ($Z = 39$) are remarkably different, as reflected in their very different zero-pressure bulk moduli (2.5 GPa and 47 GPa, respectively), but at 30 GPa, within the $tI4$ phase, the atomic volume of Rb and Y not only become the same (22.1 Å^3/atom), but they then remain the same up to 100 GPa where Y undergoes a 1.8 % volume change at its $hR24 \rightarrow oF16$ transition, which is accompanied by a change in Y's electronic structure and its compressibility [26].

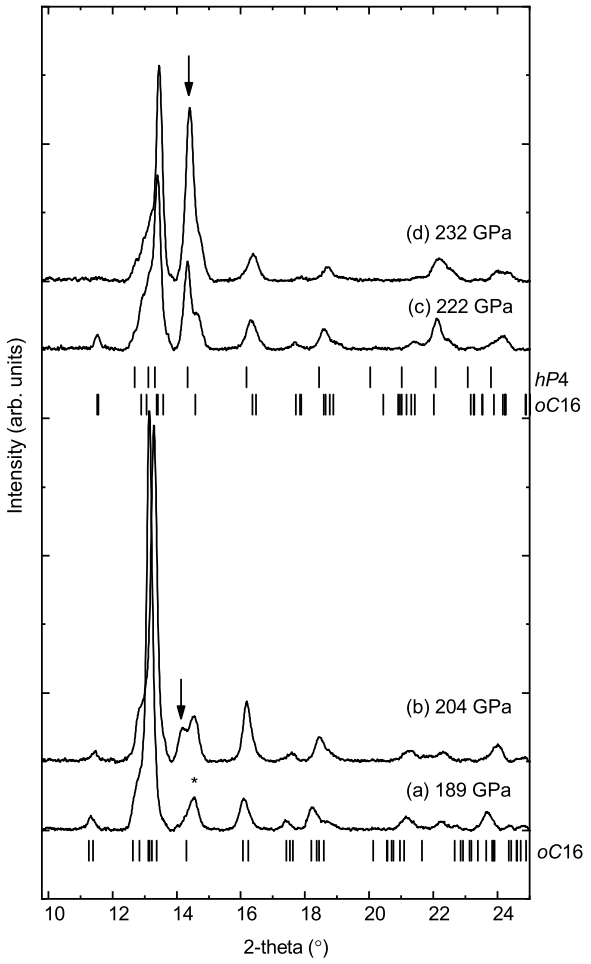

FIG. 3. Background-subtracted diffraction profiles obtained from Rb on pressure increase above (a) 189 GPa, where the sample is in the $oC16$ phase (see Fig. 2). On pressure increase to (b) 204 GPa the appearance of a new peak (identified with an arrow in (b) and (d)) marks the transition to $hP4$. On further pressure increase to (c) 222 GPa and (d) 232 GPa the peaks from $hP4$ increase in intensity, but peaks from $oC16$ were still visible at the highest pressure reached, 264 GPa. The tick marks beneath profile (a) show the calculated peak positions of $oC16$ at this pressure, while the tick marks beneath pattern (c) similarly indicate those of the $oC16$ and $hP4$ (*dhcp*) phases. The pressures in this sample were determined from the lattice parameters via the EoS determined from the other samples. The peak marked with an asterisk in profile (a) is from the Re gasket. All patterns were collected over 60 s.

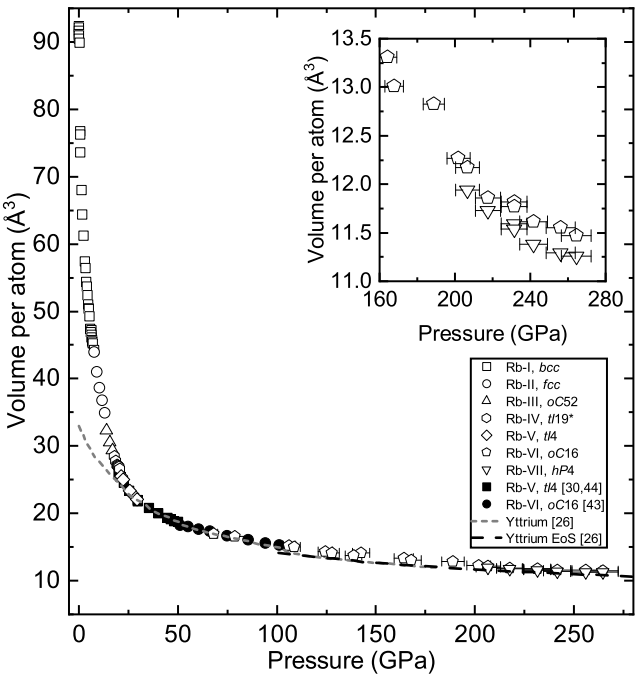

FIG. 4. The compression curve of Rb to 264(8) GPa with data from the different phases identified by the different symbols. The filled symbols are data reproduced from Refs. [30, 43, 44], and the dashed lines are the compression data and the extrapolated EoS of yttrium from Ref. [26]. The inset shows the measured volumes of the $oC16$ and $hP4$ phases above 200 GPa, illustrating the volume change of 2.3(5) % that occurs at the phase transition. The uncertainties on the volume, and those on the pressure below 100 GPa, are smaller than the symbols used to plot the data and have been omitted. The uncertainties in pressure above 100 GPa, as determined from the diamond edge scale, are ±3 % [38–40].

C. Linearization & Analysis

To fit the compression data, the Adapted Polynomial of order L (APL) EoS formalism was used [53, 54]:

$$P(x) = 3K_0\frac{(1-x)}{x^5}e^{(c_0(1-x))}\left(1 + x\sum_{k=2}^{L} c_k(1-x)^{k-1}\right) \quad (1)$$

where K_0 is the zero-pressure bulk modulus, K' is its pressure derivative, $x = (V/V_0)^{1/3}$, $c_0 = -ln(3K_0/P_{FG0})$, $c_2 = (3/2)(K'-3) - c_0$, c_k are independent fitting parameters for $k \in [3..L]$, $P_{FG0} = a_{FG0}(Z/V_0)^{(5/3)}$ is the Fermi-gas pressure, Z is the atomic number, and $a_{FG0} = 2337\,\text{GPa}\,\text{Å}^5$ is a constant. Note that in the lowest-order AP1 ($L = 1$) case, the summation term is zero and the only refinable parameters are the ambient volume (V_0) and bulk-modulus (K_0), with K' being calculated from $K' = 3 + (2/3)c_0$.

In discussing the compressive behavior of elements with very high or very low bulk moduli it is instructive to linearize the compression curve to accentuate changes in behavior. This is particularly informative for Rb which exhibits both very high compressibility at low pressure and very low compressibility at high pressure. In the APL formalism this linearization results in:

$$\eta_{APL}(x) = ln\left(\frac{Px^5}{P_{FG0}\,[1-x]}\right) \quad (2)$$

with variables and constants as in Eq. 1. In this work, in order to better realize differences in behavior to the "ideal" compressive behavior defined below, it is convenient to transform this linearization into σ-space, where $\sigma = \sigma_0 x$ and σ_0 is the Thomas-Fermi radius $(3ZV_0/4\pi)^{1/3}$.

For full details of this method see [54], but in the APL formalism an "ideal" or "simple" metal is well-described by a first-order AP1 EoS which appears as a linear plot with

$$\lim_{\sigma\to\sigma_0} \eta_{APL}(\sigma) = ln\left(\frac{3K_0}{P_{FG0}}\right) \tag{3}$$

and

$$\lim_{\sigma\to 0} \eta_{APL}(\sigma_0) = 0 \tag{4}$$

Further distinction can be made between "regular" and "irregular" EoSs, such that behavior can be classified as follows [55]

- Ideal materials, e.g. Al, exhibit linear behavior and are well described by an AP1 EoS with a slope equal to an *ideal* value calculated solely from the ambient volume and the atomic number.
- Simple materials, e.g. Cu or Au, also exhibit linear behavior and are well described by an AP1 EoS, but the slope of the line is non-ideal.
- Regular materials exhibit *slightly* non-linear behavior, indicative of higher-order APL ($L >= 2$) equations but with *small* values of c_2.
- Irregular materials, e.g. Sm, exhibit *strongly* non-linear behavior and require higher-order APL ($L >= 2$) EoSs with *large* values of c_2 and higher order terms.

The linearized data for Rb are shown in Fig. 5. Note that this type of plot is best 'read' from right to left, with increasing pressure. In the ultra-low pressure domain (<0.6 GPa), the highly non-linear nature of $\eta_{APL}(\sigma)$ yields significant uncertainties even though $\Delta P/P < 1\%$. This makes the linearized behavior difficult to interpret below $P = 0.63$ GPa ($\sigma > 9$). However, above this, the *bcc* phase exhibits linear behavior, although with a non-ideal gradient and without the correct limiting behavior of $\lim_{\sigma\to 0} \eta_{APL}(\sigma) = 0$. The transition to the *fcc* phase marks a clear shift in compressive behavior with $\eta_{APL}(\sigma)$ *decreasing* with pressure, a trend that continues monotonically in the $oC52$ and $tI19$* phases. This downward turn of $\eta_{APL}(\sigma)$ signifies a *softening* or reduction in stiffness relative to that observed in the *bcc* phase.

The transition to the $tI4$ phase at 20 GPa ($\sigma = 6.1$ Å) does not itself mark any change in the compressive behavior. However, starting at 25 GPa ($\sigma = 5.9$ Å), within the $tI4$ phase, there is a marked change in compression such that at 30 GPa and above, in the $tI4$, $oC16$ and $hP4$ phases, Rb exhibits "simple" linear compressive behavior with a gradient of $-0.75(2)$ Å^{-1}, close to the "ideal" gradient of -0.663 Å^{-1} and with the correct theoretical limit of $\eta_{APL}(0) = 0$ (see Fig. 5). We note that 30 GPa is exactly the same pressure at which the compression curves of Rb and Y meet (see Fig. 4), confirming that this is indeed a transition point for the material. This is in line with recent DFT results which show that the *s*-character of the electronic wave functions begins to decrease in Rb at 20 GPa, with the *d*-character correspondingly increasing [20]. These changes accelerate with pressure up to 27 GPa, after which the band hybridization slows but continues up to at least 40 GPa. Our data thus support the conclusion that the *s*-*d* charge transfer is most apparent in the range 20 to 30 GPa, beyond which the dominance of the *d*-bands cause Rb to behave more like a classic *d*-type metal.

Rb continues to exhibit the compressibility of a "simple" metal up to the highest pressure reached in this study, 264(8) GPa, where the volume of the $hP4$ phase is 11.29 Å^3/atom, corresponding to a V/V_0 of 0.121 or 8.26-

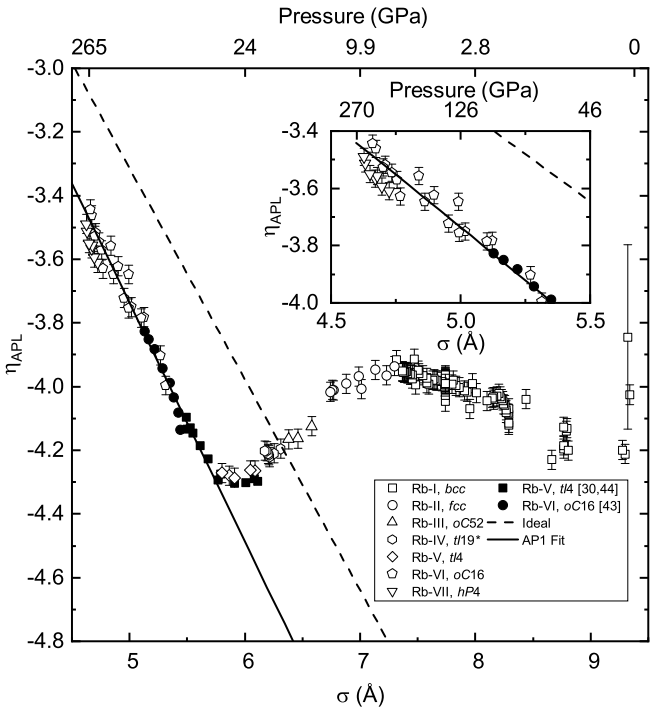

FIG. 5. Linearization of the compressibility of Rb in the form of an $\eta_{APL} - \sigma$ plot, where $\sigma = \sigma_0 x$. The data from the different phases of Rb obtained in this study are plotted using different unfilled symbols, while the filled symbols are data taken from Refs. [30, 43, 44]. Note that pressure increases non-linearly from right to left. Due to the non-linear nature of the horizontal axes the high-pressure domain occupies a disproportionately small area of the plot. The inset therefore shows an enlarged view of the pressure range 50-270 GPa. The solid line shows the best-fitting AP1 EoS to the data above 30 GPa and the dashed line is the ideal AP1 EoS for Rb.

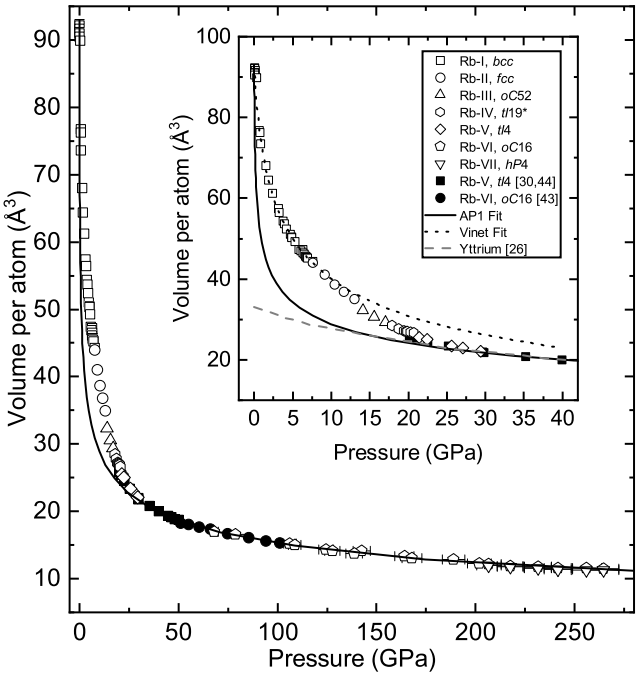

FIG. 6. The compressibility of Rb to 264 GPa (symbols) and the best-fitting AP1 EoS (solid line) to $tI4$ and $oC16$ from 30 to 264 GPa, the parameters of which are given in Table IV. It is clear that this simple EoS accurately captures the compression behavior of Rb above 30 GPa, including that of the $oC16$ phase. The inset shows an enlarged view of the data and AP1 fit up to 40 GPa, as well as the Vinet fit to the *bcc* data (dotted line) and compression data of Y for comparison (dashed line - Ref. [26]). The *bcc* phase is less compressible than predicted by the AP1 EoS, while the *fcc* phase is more compressible. As a result, the EoS and the data coincide above 30 GPa.

fold compression. This is the highest volume-compression ratio yet achieved in a metal, and second only to x-ray measurements performed on hydrogen at a $V/V_0 \sim 0.094$ at 190 GPa [56]. For comparison, recent laser compression experiments on Sn and Fe at the National Ignition Facility to 1.2 TPa and 1.4 TPa, respectively, resulted in 'only' ∼3.1- and ∼2.5-fold volume compressions [57, 58].

While both the $oC16$ and $hP4$ phases coexist above 201 GPa and both are plotted in Fig. 5, neither shows a divergence from linear behavior implying no significant changes in electronic structure at the transition between them. The linearity of the compression above 30 GPa shown in Fig. 5 means that extrapolation to higher pressures is straightforward and we estimate that a pressure of ∼530 GPa is required to reach 10-fold compression in Rb.

The linear behavior exhibited by Rb above 30 GPa in Fig. 5 lends credence to the assertion that "simple" compressive behavior is seen in elements that either do not undergo pressure-induced changes in electronic structure such as Cu and Au, or in elements that *do* undergo such changes but only once they are complete, such as we have recently reported in Sm and Y where regular behavior was observed above 65 GPa and 100 GPa, respectively [26, 37].

D. Equations of State

Attempts to fit a single EoS to the compressibility data from Rb below 30 GPa were unsuccessful; various formalisms were trialed but the irregular behavior illustrated in Fig. 5, particularly the sharp bend at the *bcc-fcc* transition, made it impossible to model the compression curve accurately. However, above 30 GPa the behavior can be modeled with the two-parameter AP1 EoS with $V_0 = 91(5)$ Å^3/atom and $K_0 = 0.17(4)$ GPa, giving a calculated $K' = 7.62(16)$. While this ambient volume is in good agreement with the $V_0 = 92.9(4)$ Å^3/atom found from the fitting the *bcc* phase alone, it has a substantial (±5 Å^3) due to the absence of data below 30 GPa, and the resulting large correlation between V_0 and K_0. For this reason, we instead chose to fix the ambient volume to $V_0 = 92.9(4)$ Å^3/atom, the value determined from fitting the data below 7 GPa, and then fitted *only* K_0 to reduce the uncertainty on both parameters.

The resulting fits to both the linearized and standard $P - V$ compression data for the $tI4$ and $oC16$ phases between 30-264 GPa are shown in Figs. 5 and 6, respectively, with best-fitting parameters shown in Table IV. As expected, the fit is excellent above 30 GPa in each case.

However, the AP1 value of $K_0 = 0.15(3)$ GPa, as determined from the ambient pressure electron density, is more than 15-times smaller than the experimental value of 2.46 GPa (see Section III B). The quality of the fit of the AP1 EoS to the experimental data below 40 GPa is highlighted in the inset to Fig. 6 and, as expected, it greatly overestimates the compression of the *bcc* phase. However, the inset also highlights the clear change in compression that occurs at the *bcc-fcc* transition at 7.6 GPa, after which Rb is *more* compressible than expected. This change is perhaps most evident in the fit of the Vinet EoS to the *bcc* phase shown in the inset to Fig. 6, where the experimental data for the *fcc* phase drop below the extrapolated Vinet EoS. In other words, the *fcc* phase is more compressible than the *bcc* phase. The subsequent *fcc*→$oC52$ transition at 13.6 GPa decreases the stiffness further, until 30 GPa where another change in compressive behavior aligns the experimental $P - V$ curve with the AP1 EoS. This reduction in stiffness at 7.6 GPa corresponds to the decrease in η_{APL} in the *fcc* and $oC52$ phases evident in Fig. 5. Thus while the AP1 EoS does not capture the complexity of behavior of low-pressure phases of Rb, it is remarkably accurate across the 30-264 GPa range.

Phase(s)	EoS	P (GPa)	V_0 (Å^3/atom)	K_0 (GPa)	K'
bcc	Vinet	<7	92.9(4)	2.46(7)	4.12(6)
$tI4$-$oC16$	AP1	30-264	-	0.15(3)	7.66(15)

TABLE IV. The parameters of the Vinet and AP1 EoSs fitted in this work. For the high-pressures phases $tI4$ & $oC16$, the ambient volume (V_0) was fixed to the value obtained from the Vinet fit to the *bcc* phase while K' was calculated from the values of Z, V_0 and K_0 [54, 55].

IV. CONCLUSIONS

In summary, we have presented a 2.5-fold extension of the phase diagram of Rb up to 264(8) GPa. We have confirmed the transition to the $hP4$ phase, starting at 207(6) GPa, as expected from analogous behavior in Cs and DFT calculations, which predicted the transition at 143 GPa. The $oC16 \rightarrow hP4$ transition is slow relative to earlier phase transitions, and diffraction peaks from the $oC16$ phase were observed to the highest pressure reached. This sluggishness matches the analogous transition in Cs [32].

Examination of the compressive behavior of Rb indicates a tendency towards d-like compression above 25 GPa, an observation which supports the assertion that d-like electronic states dominate at ultra-high pressures. The sharp change in compressibility noted within the $tI4$ phase at 30 GPa marks a definite point where the d-character of the electronic structure becomes pronounced enough to determine the compressive behavior. It is noteworthy that this is also the pressure where the compression curves of Rb ($Z = 37$) and Y ($Z = 39$) coincide, indicating that these two are analogues of each other at high pressures. The regular d-like behavior of Rb subsequently persists up to a compression ratio of $V/V_0 = 0.121$, the highest yet observed in any metal using x-ray diffraction.

Knowledge of the alkali metals' behavior at the ultra-high compressions that are typically unachievable in other elemental metals has important implications for extreme states of matter, including high density hydrogen [59], another Group I element. Research on these high-density states of matter has the potential to lead to a new view of the periodic table and the discovery and control of new material properties both at extreme and ambient conditions.

ACKNOWLEDGMENTS

British Crown Owned Copyright 2021/AWE. Published with permission of the Controller of Her Britannic Majesty's Stationery Office. This work was supported by Grant No. EP/R02927X/1 from the U.K. Engineering and Physical Sciences Research Council (EPSRC) and experimental facilities made available by Diamond Light Source (DLS). We also acknowledge DESY (Hamburg, Germany), a member of the Helmholtz Association HGF, for the provision of experimental facilities. The research leading to this result has been supported by the project CALIPSOplus under the Grant Agreement 730872 from the EU Framework Programme for Research and Innovation HORIZON 2020. We would like to thank H-P. Liermann, K. Glazyrin and R. Husband for their assistance on the P02.2 beamline at PETRA III, and D. Daisenberger for his support on the I15 beamline at DLS. S. E. Finnegan, J. D. McHardy and C. V. Storm are grateful to AWE for the award of CASE studentships. The preparation of this manuscript has benefited greatly from discussions with W. B. Holzapfel about the APL EoS formalism.

[1] E. Wigner and F. Seitz, Physical Review **43**, 804 (1933).
[2] E. Wigner and F. Seitz, Physical Review **46**, 509 (1934).
[3] Y. Ma, M. Eremets, A. R. Oganov, Y. Xie, I. Trojan, S. Medvedev, A. O. Lyakhov, M. Valle, and V. Prakapenka, Nature **458**, 182 (2009).
[4] M. I. McMahon, R. J. Nelmes, U. Schwarz, and K. Syassen, Physical Review B **74**, 140102(R) (2006).
[5] M. I. McMahon, S. Rekhi, and R. J. Nelmes, Physical Review Letters **87**, 055501 (2001).
[6] H. Jones, Proceedings of the Royal Society of London. Series A - Mathematical and Physical Sciences **147**, 396 (1934).
[7] N. F. Mott and H. Jones, *The Theory of Metals and Alloys* (Clarendon, Oxford, 1936).
[8] J. B. Neaton and N. W. Ashcroft, Nature **400**, 141 (1999).
[9] J. B. Neaton and N. W. Ashcroft, Physical Review Letters **86**, 2830 (2001).
[10] B. Rousseau and N. W. Ashcroft, Physical Review Letters **101**, 046407 (2008).
[11] P. Söderlind, O. Eriksson, B. Johansson, J. M. Wills, and A. M. Boring, Nature **374**, 524 (1995).
[12] W. Hume-Rothery, Journal of the Institute of Metals **35**, 319 (1926).
[13] G. J. Ackland and I. R. Macleod, New Journal of Physics **6**, 1 (2004).
[14] V. F. Degtyareva, Physics-Uspekhi **49**, 369 (2006).
[15] V. F. Degtyareva and O. Degtyareva, New Journal of Physics **11**, 063037 (2009).
[16] V. F. Degtyareva, Solid State Sciences **36**, 62 (2014).
[17] M. Ross and A. K. McMahan, Physical Review B **26**, 4088 (1982).
[18] L. J. Parker, T. Atou, and J. V. Badding, Science **273**, 95 (1996).
[19] G. Fabbris, J. Lim, L. S. I. Veiga, D. Haskel, and J. S. Schilling, Physical Review B **91**, 085111 (2015).
[20] G. Woolman, V. Naden Robinson, M. Marqués, I. Loa, G. J. Ackland, and A. Hermann, Physical Review Mate-

rials **2**, 053604 (2018).
[21] A. K. McMahan, Physical Review B **29**, 5982 (1984).
[22] M. I. McMahon and R. J. Nelmes, Chemical Society Reviews **35**, 943 (2006).
[23] Y. Akahama, H. Fujihisa, and H. Kawamura, Physical Review Letters **94**, 195503 (2005).
[24] K. Takemura and K. Syassen, Journal of Physics F: Metal Physics **15**, 543 (1985).
[25] M. I. McMahon, T. Bovornratanaraks, D. Allan, S. Belmonte, and R. Nelmes, Physical Review B **61**, 3135 (2000).
[26] E. J. Pace, S. E. Finnegan, C. V. Storm, M. Stevenson, M. I. McMahon, S. G. MacLeod, E. Plekhanov, N. Bonini, and C. Weber, Physical Review B **102**, 094104 (2020).
[27] M. S. Miao and R. Hoffmann, Journal of the American Chemical Society **137**, 3631 (2015).
[28] Y. Deng and J. S. Schilling, Physical Review B **100**, 041109(R) (2019).
[29] L. F. Lundegaard, M. Marqués, G. Stinton, G. J. Ackland, R. J. Nelmes, and M. I. McMahon, Physical Review B **80**, 020101(R) (2009).
[30] U. Schwarz, K. Syassen, A. Grzechnik, and M. Hanfland, Solid State Communications **112**, 319 (1999).
[31] U. Schwarz, K. Takemura, M. Hanfland, and K. Syassen, Physical Review Letters **81**, 2711 (1998).
[32] K. Takemura, N. E. Christensen, D. L. Novikov, K. Syassen, U. Schwarz, and M. Hanfland, Physical Review B **61**, 14399 (2000).
[33] Y. Ma, A. R. Oganov, and Y. Xie, Physical Review B **78**, 014102 (2008).
[34] R. D. Shannon, Acta Crystallographica Section A **32**, 751 (1976).
[35] R. Boehler and K. De Hantsetters, High Pressure Research **24**, 391 (2004).
[36] A. Dewaele, P. Loubeyre, and M. Mezouar, Physical Review B **70**, 094112 (2004).
[37] S. E. Finnegan, E. J. Pace, C. V. Storm, M. I. McMahon, S. G. MacLeod, H.-P. Liermann, and K. Glazyrin, Physical Review B **101**, 174109 (2020).
[38] Y. Akahama and H. Kawamura, Journal of Applied Physics **96**, 3748 (2004).
[39] Y. Akahama and H. Kawamura, Journal of Applied Physics **100**, 043516 (2006).
[40] Y. Akahama and H. Kawamura, in *Journal of Physics: Conference Series*, Vol. 215 (2010) p. 012195.
[41] See Supplemental Material at [LINK] for additional information on the diamond edge spectroscopy, pressure distribution on the culet, and details on the low-pressure Vinet EoS, which includes Refs. [36, 39, 40, 42, 49, 51, 60].
[42] S. Anzellini, A. Dewaele, F. Occelli, P. Loubeyre, and M. Mezouar, Journal of Applied Physics **115**, 043511 (2014).
[43] S. D. Panfilis, F. Gorelli, M. Santoro, L. Ulivi, E. Gregoryanz, T. Irifune, T. Shinmei, I. Kantor, O. Mathon, S. Pascarelli, S. D. Panfilis, F. Gorelli, M. Santoro, L. Ulivi, E. Gregoryanz, T. Irifune, and T. Shinmei, The Journal of Chemical Physics **142**, 214503 (2015).
[44] U. Schwarz, A. Grzechnik, K. Syassen, I. Loa, and M. Hanfland, Physical Review Letters **83**, 4085 (1999).
[45] C. Prescher and V. B. Prakapenka, High Pressure Research **35**, 223 (2015).
[46] V. Petrícek, M. Dušek, and L. Palatinus, Zeitschrift für Kristallographie **229**, 345 (2014)
.
[47] T. J. B. Holland and S. A. T. Redfern, Mineralogical Magazine **61**, 65 (1997)
.
[48] R. J. Nelmes, M. I. McMahon, J. S. Loveday, and S. Rekhi, Physical Review Letters **88**, 155503 (2002).
[49] M. Winzenick, V. Vijayakumar, and W. B. Holzapfel, Physical Review B **50**, 12381 (1994).
[50] J. T. Waber and D. T. Cromer, The Journal of Chemical Physics **42**, 4116 (1965).
[51] P. Vinet, J. Ferrantef, J. R. Smith, and J. H. Rose, Journal of Physics C: Solid State Physics **19**, L467 (1986).
[52] J. Gonzalez-Platas, M. Alvaro, F. Nestola, and R. Angel, Journal of Applied Crystallography **49**, 1377 (2016).
[53] W. B. Holzapfel, Reports on Progress in Physics **59**, 29 (1996).
[54] W. B. Holzapfel, High Pressure Research **16**, 81 (1998).
[55] W. B. Holzapfel, Zeitschrift für Kristallographie **215**, 473 (2001).
[56] Y. Akahama, Y. Mizuki, S. Nakano, N. Hirao, and Y. Ohishi, Journal of Physics: Conference Series **950**, 042060 (2017).
[57] A. Lazicki, J. R. Rygg, F. Coppari, R. Smith, D. Fratanduono, R. G. Kraus, G. W. Collins, R. Briggs, D. G. Braun, D. C. Swift, and J. H. Eggert, Physical Review Letters **115**, 075502 (2015).
[58] R. F. Smith, D. E. Fratanduono, D. G. Braun, T. S. Duffy, J. K. Wicks, P. M. Celliers, S. J. Ali, A. Fernandez-Pañella, R. G. Kraus, D. C. Swift, G. W. Collins, and J. H. Eggert, Nature Astronomy **2**, 452 (2018).
[59] E. Wigner and H. B. Huntington, The Journal of Chemical Physics **3**, 764 (1935).
[60] A. Savitzky and M. J. Golay, Analytical Chemistry **36**, 1627 (1964).